PAPER

CrossMark
click for updates

T_1-Weighted MR/CT dual-modality imaging-guided photothermal therapy using gadolinium-functionalized triangular gold nanoprism†

Wenfei Liu,[a] Kai Liu,[b] Ying Zhao,[a] Shuang Zhao,[a] Song Luo,[a] Ying Tian,[a] Zhaogang Teng,*[a] Shouju Wang*[a] and Guangming Lu*[a]

Multifunctional nanoagents, in particular those that combine diverse diagnostic and therapeutic functions, have attracted great enthusiasm in oncotherapy. In this work, a triangular gold nanoprism decorated with gadopentetic acid (Gd–DTPA) (TGP–PEG–Gd) was constructed for use in cancer theranostics. TGP–PEG–Gd exhibits uniform morphology, excellent monodispersity and near infrared absorbance properties. The magnetic properties of gadolinium, together with the X-ray attenuation of gold, enable TGP–PEG–Gd to be employed for T_1-weighted MR/CT dual-modality imaging. The longitudinal relaxivity (r_1) of TGP–PEG–Gd was calculated to be 23.1 mM^{-1} s^{-1}, and its X-ray absorption coefficient was 959.3 HU L g^{-1}. In addition, TGP–PEG–Gd possesses effective photothermal conversion ability, which was utilized for successful photothermal therapy. Moreover, the excellent biocompatibility of TGP–PEG–Gd was proved both *in vitro* and *in vivo*. Biocompatible TGP–PEG–Gd may hold promise for the photothermal therapy of cancers guided by MR/CT dual-modality imaging.

Introduction

Photothermal therapy (PTT) holds promise in the area of anti-tumour therapy owing to its precise delivery of energy, minimal invasiveness, and high spatiotemporal selectivity in comparison to conventional tumour treatment modalities.[1–6] Imaging-guided PTT, which combines single or multiple imaging modalities with PTT, has attracted ever-increasing interest.[7–10] With the development of nanotechnology, the integration of the detection of lesions, hyperthermal ablation and monitoring of therapeutic efficacy within a single nano-platform could dramatically simplify and optimize the diagnosis and treatment of tumours.[3,7,11–13]

Among the various tumour imaging modalities, computed tomography (CT) and magnetic resonance imaging (MRI) are the most widely used in clinical applications owing to their high resolution and deep penetration.[14,15] Moreover, each of these modalities has its own characteristics. MR imaging provides outstanding soft tissue contrast but has defects in revealing calcifications. On the other hand, CT provides better density resolution and is preferable for the imaging of osseous tissue

and calcifications.[14,16,17] The combination of MRI and CT could combine their merits and overcome their defects and thus achieve accurate diagnosis of tumours and provide precise guidance for PTT.[16,18,19]
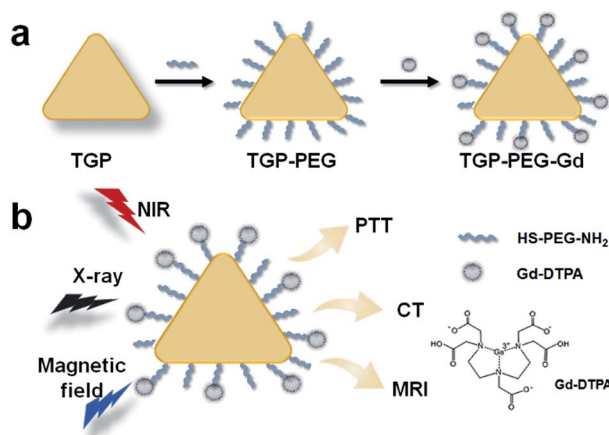
However, a limited number of studies have investigated the employment of nanoplatforms for PTT guided by MR/CT. One reason for this is that such nanoplatforms need to contain several different components, including X-ray attenuation elements (*e.g.*, iodine and bismuth) for CT, magnetic materials (*e.g.*, iron oxide and manganese selenide) for MR, and photothermal conversion materials (*e.g.*, carbon nanotubes and graphene) for PTT.[3,6,7] Their sophisticated assembly, challenging synthesis, and uncertain stability have significantly hindered the employment of these nanoplatforms.[19,20] Moreover, most such nanoplatforms are designed for T_2-weighted MR imaging.[14,18,19] However, T_1-weighted MR imaging plays an equally important role in the clinical diagnosis of cancer. Thus, it is urgently necessary to develop novel nanostructures that inherently combine T_1-weighted MR/CT imaging and photothermal conversion capacities and have a facile synthesis strategy.

Gold nanostructures have attracted great interest in biomedical applications.[21,22] Owing to their strong absorption in the near infrared (NIR) region and outstanding photothermal conversion capacity, gold nanostructures are suitable candidates for PTT.[23–26] In addition, as a high-Z element, gold has a large X-ray attenuation coefficient, which enables it to perform CT enhancement.[14,15] Moreover, by simple chemical modification gold nanostructures can be decorated with various

[a]Department of Medical Imaging, Jinling Hospital, Medical School of Nanjing University, Nanjing 210002, P. R. China. E-mail: tzg@fudan.edu.cn; shouju.wang@gmail.com; cjr.luguangming@vip.163.com

[b]Nanjing Stomatological Hospital, Medical School of Nanjing University, Nanjing 210008, P. R. China.

† Electronic supplementary information (ESI) available. See DOI: 10.1039/c7ra01101f

Scheme 1 Schematic representation of the fabrication of TGP–PEG–Gd and PTT guided by T_1-weighted MR/CT dual-modality imaging.

functional groups, such as gadolinium compounds, to achieve MR imaging.

Here, as shown in Scheme 1, we introduced a multifunctional nanoagent based on triangular gold nanoprisms (TGP) decorated with gadopentetic acid (Gd–DTPA) by simple covalent bonding (denoted as TGP–PEG–Gd). The gold nanoconjugate was proved to display excellent performance in T_1-weighted MR and CT enhancement and efficacy in photothermal therapy. Moreover, the nanoconjugate displayed negligible acute toxicity both *in vitro* and *in vivo*, which further confirmed its potential for medical applications in PTT guided by T_1-weighted MR/CT dual-modality imaging.

Experimental

Materials

Hexadecyltrimethylammonium chloride (CTAC) was purchased from TCI (Shanghai, China). Hydrogen tetrachloroaurate trihydrate (HAuCl$_4$·3H$_2$O), potassium iodide (KI), L-ascorbic acid, *N*-(3-dimethylaminopropyl)-*N*′-ethylcarbodiimide hydrochloride (EDC), and *N*-hydroxysulfosuccinimide sodium salt (sulfoNHS) were purchased from Sigma-Aldrich (St. Louis, MO, USA). Sodium hydroxide (NaOH) was purchased from Sinopharm Chemical Reagent Co. Ltd (Shanghai, China). Phosphate-buffered saline (PBS) and cell counting kit-8 (CCK-8) were purchased from Keygen Biotech (China). Thiol–PEG–amine (HS–PEG–NH$_2$, M.W. ≈ 1000 Da) was purchased from Laysan Bio Inc. Gd–DTPA was purchased from Guangzhou Consun Pharmaceutical Group Ltd (China). All chemicals were used without further treatment.

Synthesis and purification of TGP

TGP was fabricated by seedless oxidative etching, as previously reported.[27,28] Firstly, 240 μL of 25.4 mM HAuCl$_4$ and 61 μL of 0.1 M NaOH were mixed to form solution A. Solution A was added to a 10 mL aqueous solution that contained 16 mM CTAC and 0.75 mM KI. Then, 100 μL of 64 mM ascorbic acid was injected into the resulting solution. Finally, 5 μL of 0.1 M NaOH was injected into the solution with rapid shaking. After the completion of the growth process, purification was carried out by adding 2.5 mL of 0.5 M CTAC to the system to purify TGPs from spherical by-products. After flocculation for 12 h, the supernatant was removed and the precipitates were redispersed in ultrapure water.

Preparation of TGP–PEG–Gd

Firstly, 0.5 mL TGP solution with an absorbance of 3 O.D., 0.5 mL of 4 mM HS–PEG–NH$_2$, and 4.5 mL ultrapure water were mixed and vortexed immediately. Then, the mixed solution was sonicated for 30 min to obtain amine-terminated PEGylated TGP, which was collected by centrifugation and redispersed in 1 mL ultrapure water.

In addition, 4 mL of 0.1 M Gd–DTPA solution and 1.2 mL of 1 mg mL^{-1} NHS were added to 4.8 mL PBS buffer and stirred in the dark for 2 h. After the addition of 1.8 mL of 1 mg mL^{-1} EDC·HCl, the reaction mixture was stirred for 3–4 h in the dark. Finally, 1 mL of the as-prepared solution of amine-terminated PEGylated TGP was added and the mixed solution was stirred overnight in the dark. The solution was centrifuged to collect TGP–PEG–Gd.

Characterization of TGP–PEG–Gd

Transmission electron microscopy images were acquired with a JEOL JEM-2100 microscope (Japan). UV-vis spectra were recorded using a Lambda 35 UV-vis spectrophotometer (Perkin-Elmer Instruments, USA). Hydrodynamic diameters and zeta potentials were measured with a NanoBrook ZetaPlus zeta potential analyzer (Brookhaven Instruments, USA). Electron-dispersive X-ray (EDX) spectra were recorded using a Tecnai G2 F20 microscope (FEI, Hillsboro, OR) with an EDX detector system. MR images were captured using a 3.0 T MR scanner (MAGNETOM Trio, Siemens, Germany) at room temperature. T_1 values were determined from the regions of interest in T_1 map MR images. CT images were recorded using a dual-source CT system (Somatom Definition, Siemens Healthcare, Forchheim, Germany) with a slice thickness of 5 mm and a voltage of 120 kVp. The X-ray attenuation was measured in Hounsfield units (HU) on a dedicated workstation (Multi Modality Workplace, Siemens Medical Solutions, Erlangen, Germany). A 660 nm diode-pumped laser source was obtained from Hi-Tech Opto-electronics Co. Ltd (China). Infrared thermal images were acquired using an infrared camera (MAGNITY f15F1, Wuhan VST Light & Technology Co., Ltd (China)).

Calculation of photothermal conversion efficiency

The photothermal conversion efficiency was calculated by a previously reported method[29] according to the following equation:

$$\eta = \frac{hS(T_{max} - T_{amb}) - Q_0}{I(1 - 10^{-A})}$$

After the thermal input and output attained equilibrium, the value of hS could be determined according to the following equation:

$$hS = \frac{\sum m_i C_{p,i}}{\tau_s} \approx \frac{m_{H_2O} C_{H_2O}}{\tau_s}$$

The value of τ_s was determined during the cooling stage using the following equation:

$$t = -\tau_s \ln \theta = -\tau_s \ln \frac{T - T_{amb}}{T_{max} - T_{amb}}$$

In vitro cell viability assays

The MDA-MB-231 human breast cancer cell line was chosen for *in vitro* studies. The cells were cultured in 96-well plates for 24 h. TGP–PEG–Gd was injected into the culture medium at concentrations ranging from 0.6 to 10 µg mL^{-1}, and the cells were incubated for another 24 h. The cell viability was measured by assays with cell counting kit-8 (CCK-8) in accordance with the manufacturer's instructions. The cells were irradiated with an NIR laser (660 nm, 1.0 W cm^{-2}, 5 min), followed by a CCK-8 assay to determine the phototherapeutic efficacy of the nanoconjugate.

Evaluation of in vivo biocompatibility

Two groups of nude mice (6–8 weeks old, $n = 3$) were intravenously injected with 100 µL normal saline and a solution of TGP–PEG–Gd with an Au concentration of 100 µg mL^{-1}, respectively. After 24 h, the mice were sacrificed and their major organs (including hearts, livers, spleens, lungs, and kidneys) were collected for staining with hematoxylin and eosin (H&E). The animal experiments were carried out in accordance with the guidelines of Jinling Hospital, Nanjing, China, and were approved by the Institutional Animal Care and Use Committee of Jinling Hospital.

Results and discussion

Bare TGP was synthesized by seedless oxidative etching, in which CTAC served as the surfactant. To enable photothermal therapy in the NIR region, the side length of TGP was adjusted to 80.4 ± 4.3 nm (Fig. 1a) by controlling the NaOH concentration. The corresponding localized surface plasmon resonance (LSPR) displayed a peak at 640 nm (Fig. 1b). Bare TGP exhibited a uniform triangular morphology and excellent monodispersity, as shown in the TEM image. The hydrodynamic diameter of bare TGP was determined to be 48.5 ± 1.2 nm by dynamic light scattering measurements (Fig. 1c), which was slightly smaller
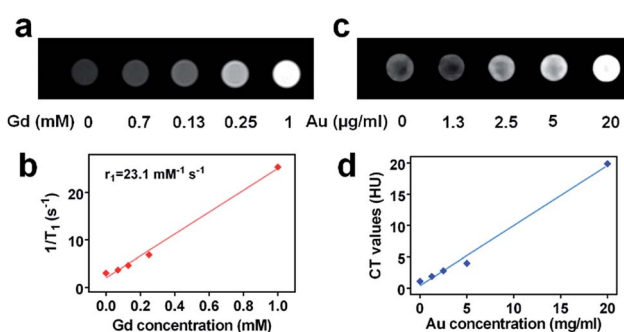
Fig. 2 (a) T_1-Weighted MR images of TGP–PEG–Gd solutions. (b) Linear fitting of $1/T_1$ values as a function of the Gd concentration. (c) CT images of TGP–PEG–Gd solutions. (d) Linear fitting of CT values (HU) as a function of the Au concentration.
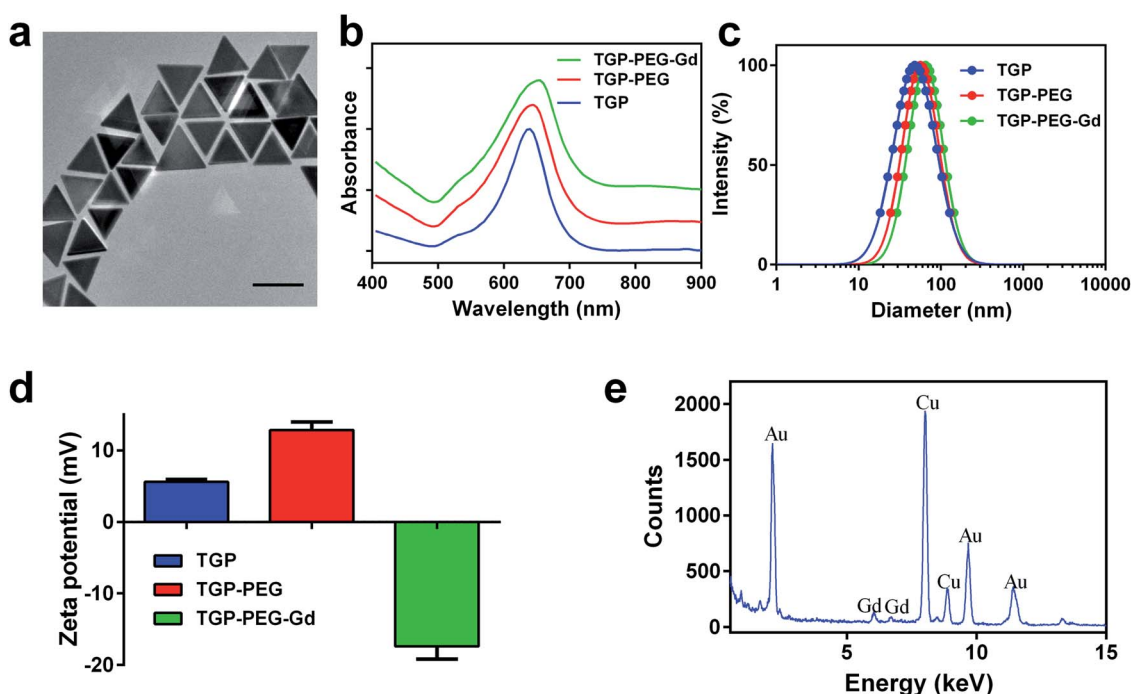
Fig. 1 (a) TEM image of TGP (scale bar: 100 nm). (b) UV-vis spectra, (c) distribution of hydrodynamic diameters and (d) zeta potentials of TGP, TGP–PEG, and TGP–PEG–Gd. (e) EDX spectrum of TGP–PEG–Gd.
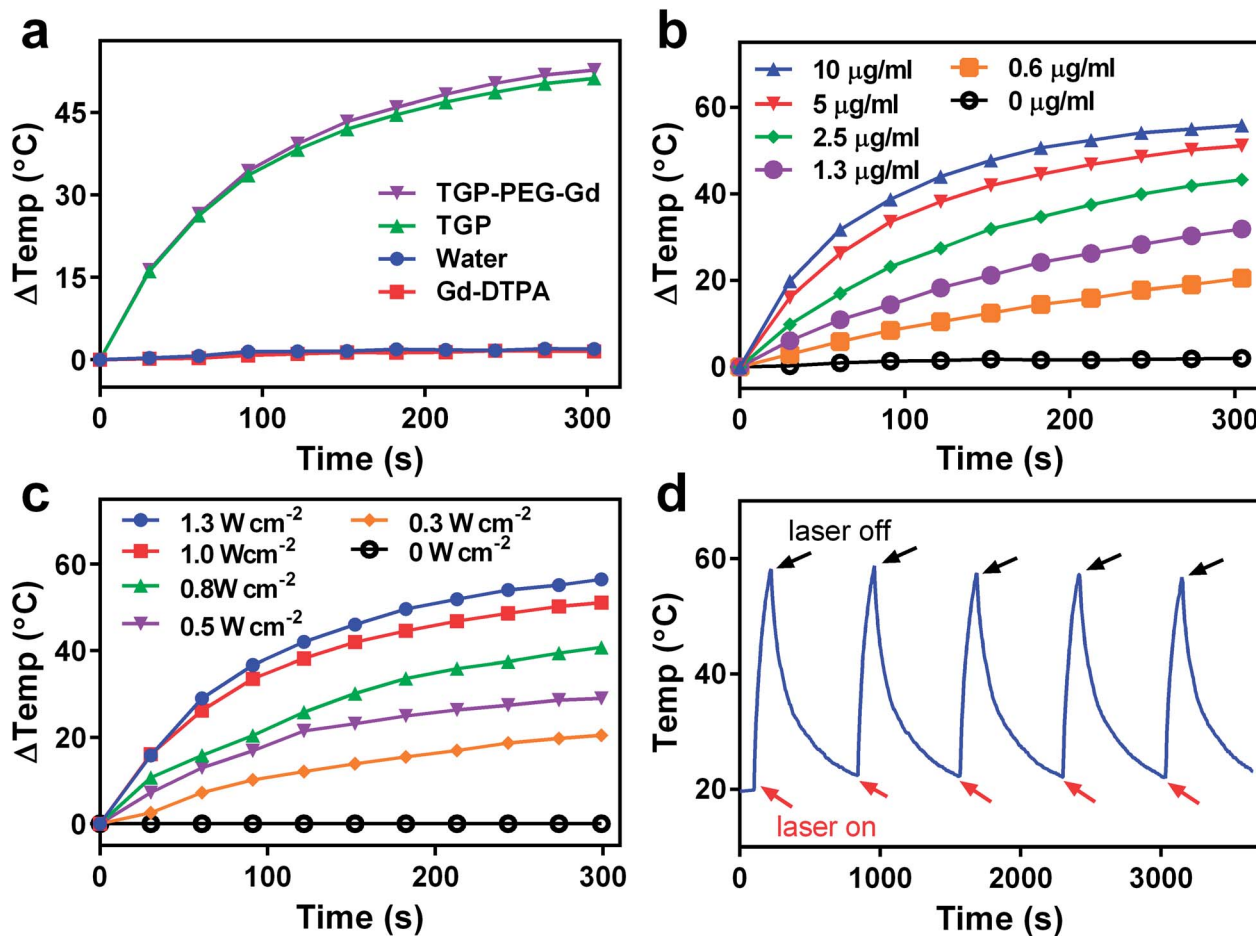
Fig. 3 (a) Heating curves of ultrapure water, 5 μg mL^{-1} TGP, and the corresponding concentrations of TGP–PEG–Gd and Gd–DTPA irradiated with a 660 nm laser (1.0 W cm^{-2}, 5 min). (b) Heating curves of TGP–PEG–Gd solutions with different Au concentrations. (c) Heating curves of TGP–PEG–Gd solution with an Au concentration of 5 μg mL^{-1} at different power densities. (d) Heating–cooling curve of TGP–PEG–Gd solution with an Au concentration of 5 μg mL^{-1} (irradiated with a 660 nm laser at 1.0 W cm^{-2} for 2 min and cooled for 10 min).

than the size measured by TEM. This deviation might be attributed to the fact that rotational diffusion of bare TGP was also recorded by DLS measurements (Fig. S1†). This

phenomenon has also been reported for other anisotropic particles.[26,30] The zeta potential of bare TGP was 5.59 ± 0.32 mV (Fig. 1d).
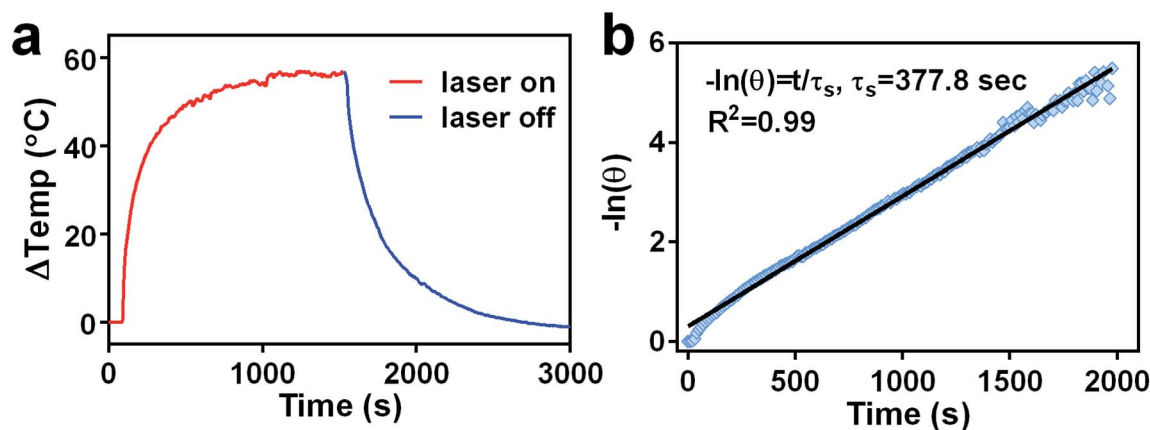

Fig. 4 (a) Heating (irradiated with a 660 nm laser at a power density of 1.0 W cm^{-2}) and cooling (without laser irradiation) curves of a solution of TGP–PEG–Gd with an Au concentration of 5 μg mL^{-1}. (b) Linear fit of the negative natural logarithm of the driving force temperature as a function of time.

Fig. 5 Relative viability of MDA-MB-231 cells treated with TGP–PEG–Gd (a) without and (b) with irradiation (660 nm, 1.0 W cm^{-2}, 5 min).

To endow TGP with MR imaging ability, bare TGP was decorated with molecules of Gd–DTPA, which is a widely used commercial MR contrast agent. Firstly, HS–PEG–NH$_2$ (M.W. $\approx$ 1000 Da) was introduced to obtain amino-functionalized PEGylated TGP (denoted as TGP–PEG). Next, Gd–DTPA was easily conjugated to TGP–PEG via the condensation reaction of amino groups and carboxyl groups (denoted as TGP–PEG–Gd). After conjugation, the UV-vis spectra exhibited a slight shift in the LSPR bands from 640 nm to 655 nm without obvious broadening of the peaks (Fig. 1b). The result suggested that TGP was successfully decorated with Gd–DTPA without obvious aggregation. The hydrodynamic diameter increased to 65.2 $\pm$ 1.5 nm (Fig. 1c) and the zeta potential was found to be -17.38 ± 1.79 mV (Fig. 1d) after decoration. The EDX spectrum clearly revealed signals of Au at 2.123, 9.712 and 11.440 keV and signals of Gd at 6.056 and 6.712 keV. The results further confirmed the successful conjugation of Gd–DTPA to TGP (Fig. 1e). The weight ratio of gold : gadolinium was measured to be 19.6 : 1 by ICP-AES.

To illustrate the multimodal imaging capacity of TGP–PEG–Gd, we first investigated its ability to perform MR enhancement. T_1-Weighted phantom MR images of solutions of TGP–PEG–Gd were captured with a 3.0 T clinical MR scanner. As shown in

Fig. 2a, the intensity of the MR signal increased progressively as the concentration of TGP–PEG–Gd increased. The T_1 relaxation rate $(1/T_1)$ was found to have a linear relationship with the concentration of TGP–PEG–Gd with a longitudinal relaxivity (r_1) of 23.1 mM^{-1} s^{-1} (Fig. 2b). Thus, TGP–PEG–Gd exhibited excellent capacity for T_1-weighted MR enhancement.

On the other hand, as gold has a higher X-ray attenuation coefficient than iodine, which is the most commonly used CT contrast element, it was expected that TGP–PEG–Gd could perform excellent CT enhancement. To investigate its enhancement ability, CT images of dispersions of TGP–PEG–Gd with various concentrations were captured. As shown in Fig. 2c, the CT attenuation of the solutions increased gradually with an increase in the concentration of TGP–PEG–Gd. By a linear fit of the values of the CT attenuation with the concentrations of TGP–PEG–Gd, the X-ray attenuation coefficient was calculated to be 959.3 HU L g^{-1} (Fig. 2d). The relatively high longitudinal relaxivity and X-ray attenuation coefficient indicated the potential use of TGP–PEG–Gd as a multimodal imaging enhancement medium.

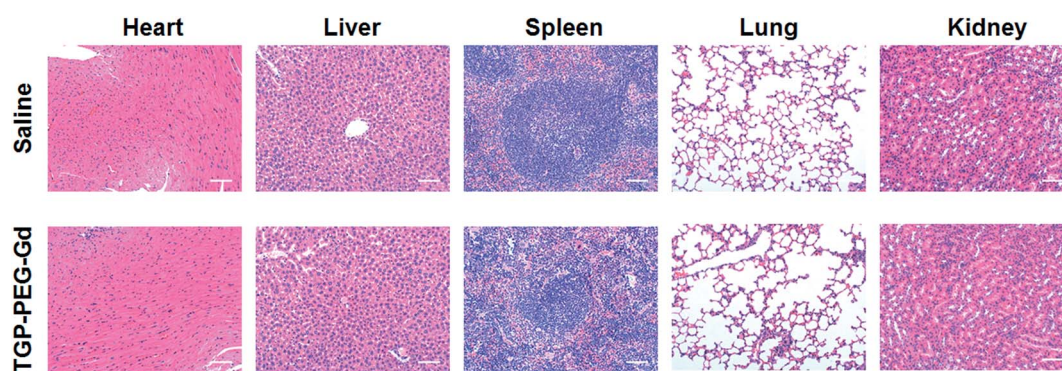Because photothermal conversion efficiency is critical for performing PTT, the photothermal performance of TGP–PEG–

Fig. 6 H&E staining images of mouse organs 24 h after injection of saline or a solution of TGP–PEG–Gd (scale bar: 50 μm).

Gd was tested systematically. Under irradiation with a 660 nm laser at 1.0 W cm^{-2}, solutions of TGP and TGP–PEG–Gd underwent rapid heating by similar amounts of 51.2 °C and 52.7 °C, respectively (Fig. 3a). The rises in temperature were sufficient for tumour ablation. Spherical gold nanoparticles (GNP) of a similar size with the same optical density were used as controls. For comparison with TGP and TGP–PEG–Gd, even though the LSPR of GNP was around 520 nm, we used the same NIR laser to irradiate the GNP solution. However, the GNP solution only underwent a rise in temperature of less than 10 °C (Fig. S2†). The Gd–DTPA solution and ultrapure water exhibited a negligible rise in temperature. Thus, the photothermal conversion was mediated by TGP and conjugation would not impair its photothermal performance. In addition, the heating curves of solutions of TGP–PEG–Gd at various concentrations and powers of the laser used for irradiation revealed that the photothermal conversion was dependent on the concentration and laser power (Fig. 3b and c, S3†). Moreover, the excellent photostability of TGP–PEG–Gd was proved by its stable photothermal conversion capacity after five heating–cooling cycles (Fig. 3d). The photothermal conversion efficiency of TGP–PEG–Gd was calculated to be 68.7% by a previously reported method (Fig. 4).

To evaluate the potential of TGP–PEG–Gd for PTT, the therapeutic efficacy of the nanoconjugate was determined using MDA-MB-231 cells. The cells were incubated with TGP–PEG–Gd at different concentrations for 24 h, followed by a CCK-8 assay. Without laser irradiation, TGP–PEG–Gd gave rise to negligible impairment of the viability of MDA-MB-231 cells. Up to 95.3% of cells survived even at the highest concentration used in the assay (Fig. 5a), which indicated that the nanoconjugate itself was harmless to the cells. However, after irradiation with an NIR laser (660 nm at 1.0 W cm^{-2} for 5 min), as shown in Fig. 5b, a noticeable amount of cell death was revealed by the CCK-8 assay. When the concentration of TGP–PEG–Gd was 10 μg mL^{-1}, only 12.6% of MDA-MB-231 cells survived after irradiation. The above results collectively suggest that TGP–PEG–Gd possesses excellent photothermal therapeutic efficacy and biocompatibility in vitro.

To further demonstrate the potential of TGP–PEG–Gd for biomedical applications, the in vivo biocompatibility of the nanoconjugate was assessed. Two groups of mice were intravenously injected with 100 μL normal saline and a solution of TGP–PEG–Gd with an Au concentration of 100 μg mL^{-1}, respectively. After 24 h, the mice were sacrificed and their major organs (including hearts, livers, spleens, lungs, and kidneys) collected for histopathological examination. Notably, the organs in both groups retained their normal histological morphology, and no obvious tissue damage or inflammation was observed (Fig. 6). The results proved that TGP–PEG–Gd possesses negligible acute toxicity in vivo at the given concentration.

Conclusions

In summary, a multifunctional platform based on triangular gold nanoprisms was constructed via a facile protocol. By decoration with Gd–DTPA, the as-prepared TGP–PEG–Gd was endowed with magnetic properties and T_1-weighted MR contrast ability. Owing to the high X-ray absorption coefficient of gold, TGP–PEG–Gd could effectively serve as a CT contrast medium. In addition, TGP–PEG–Gd exhibited high photothermal conversion efficacy, which provided the nanoconjugate with high capability for PTT. Moreover, TGP–PEG–Gd exhibited excellent biocompatibility both in vitro and in vivo. Our results suggest that TGP–PEG–Gd holds considerable promise in the use of PTT guided by MR/CT dual-modality imaging for cancer treatment. The concept of in vitro theranostics may hopefully be extended to in vivo animal experiments in further investigations.

References

1 M. Aioub, S. R. Panikkanvalappil and M. A. El-Sayed, ACS Nano, 2017, 11, 579–586.

2 H. Lin, X. Wang, L. Yu, Y. Chen and J. Shi, Nano Lett., 2017, 17, 384–391.

3 G. Feng, Y. Fang, J. Liu, J. Geng, D. Ding and B. Liu, Small, 2017, DOI: 10.1002/smll.201602807.

4 R. Singh and S. V. Torti, Adv. Drug Delivery Rev., 2013, 65, 2045–2060.

5 J. Kim, J. Kim, C. Jeong and W. J. Kim, Adv. Drug Delivery Rev., 2016, 98, 99–112.

6 H. S. Han, K. Y. Choi, H. Lee, M. Lee, J. Y. An, S. Shin, S. Kwon, D. S. Lee and J. H. Park, ACS Nano, 2016, 10, 10858–10868.

7 Z. Li, J. Liu, Y. Hu, K. A. Howard, Z. Li, X. Fan, M. Chang, Y. Sun, F. Besenbacher, C. Chen and M. Yu, ACS Nano, 2016, DOI: 10.1021/acsnano.6b05427.

8 Y. Cai, P. Liang, Q. Tang, X. Yang, W. Si, W. Huang, Q. Zhang and X. Dong, ACS Nano, 2017, 11, 1054–1063.

9 Y. W. Chen, Y. L. Su, S. H. Hu and S. Y. Chen, Adv. Drug Delivery Rev., 2016, 105, 190–204.

10 Z. Chen, P. Zhao, Z. Luo, M. Zheng, H. Tian, P. Gong, G. Gao, H. Pan, L. Liu, A. Ma, H. Cui, Y. Ma and L. Cai, ACS Nano, 2016, 10, 10049–10057.

11 W. P. Li, C. H. Su, L. C. Tsao, C. T. Chang, Y. P. Hsu and C. S. Yeh, ACS Nano, 2016, 10, 11027–11036.

12 L. Zhang, H. Su, J. Cai, D. Cheng, Y. Ma, J. Zhang, C. Zhou, S. Liu, H. Shi, Y. Zhang and C. Zhang, ACS Nano, 2016, 10, 10404–10417.

13 W. Chen, J. Ouyang, H. Liu, M. Chen, K. Zeng, J. Sheng, Z. Liu, Y. Han, L. Wang, J. Li, L. Deng, Y. N. Liu and S. Guo, Adv. Mater., 2016, DOI: 10.1002/adma.201603864.

14 Y. Hu, R. Wang, S. Wang, L. Ding, J. Li, Y. Luo, X. Wang, M. Shen and X. Shi, *Sci. Rep.*, 2016, **6**, 28325.

15 Y. Tian, S. Luo, H. Yan, Z. Teng, Y. Pan, L. Zeng, J. Wu, Y. Li, Y. Liu, S. Wang and G. Lu, *J. Mater. Chem. B*, 2015, **3**, 4330–4337.

16 H. Zhang, H. Wu, J. Wang, Y. Yang, D. Wu, Y. Zhang, Y. Zhang, Z. Zhou and S. Yang, *Biomaterials*, 2015, **42**, 66–77.

17 J. H. Kim, S. W. Park, S. C. Kim, M. K. Lim, T. Y. Jang, Y. J. Kim, Y. H. Kang and H. Y. Lee, *Korean J. Radiol.*, 2015, **16**, 566–574.

18 L. Cheng, S. Shen, S. Shi, Y. Yi, X. Wang, G. Song, K. Yang, G. Liu, T. E. Barnhart, W. Cai and Z. Liu, *Adv. Funct. Mater.*, 2016, **26**, 2185–2197.

19 G. Yang, H. Gong, T. Liu, X. Sun, L. Cheng and Z. Liu, *Biomaterials*, 2015, **60**, 62–71.

20 L. Cheng, C. Yuan, S. Shen, X. Yi, H. Gong, K. Yang and Z. Liu, *ACS Nano*, 2015, **9**, 11090–11101.

21 R. Bardhan, S. Lal, A. Joshi and N. J. Halas, *Acc. Chem. Res.*, 2011, **44**, 936–946.

22 L. Dykman and N. Khlebtsov, *Chem. Soc. Rev.*, 2012, **41**, 2256–2282.

23 S. Wang, Z. Teng, P. Huang, D. Liu, Y. Liu, Y. Tian, J. Sun, Y. Li, H. Ju, X. Chen and G. Lu, *Small*, 2015, **11**, 1801–1810.

24 S. Wang, Y. Tian, W. Tian, J. Sun, S. Zhao, Y. Liu, C. Wang, Y. Tang, X. Ma, Z. Teng and G. Lu, *ACS Nano*, 2016, **10**, 8578–8590.

25 S. Wang, P. Huang, L. Nie, R. Xing, D. Liu, Z. Wang, J. Lin, S. Chen, G. Niu, G. Lu and X. Chen, *Adv. Mater.*, 2013, **25**, 3055–3061.

26 X. Ma, Y. Cheng, Y. Huang, Y. Tian, S. Wang and Y. Chen, *RSC Adv.*, 2015, **5**, 81682–81688.

27 L. Chen, F. Ji, Y. Xu, L. He, Y. Mi, F. Bao, B. Sun, X. Zhang and Q. Zhang, *Nano Lett.*, 2014, **14**, 7201–7206.

28 L. Scarabelli, M. Coronado-Puchau, J. J. Giner-Casares, J. Langer and L. M. Liz-Marzan, *ACS Nano*, 2014, **8**, 5833–5842.

29 D. K. Roper, W. Ahn and M. Hoepfner, *J. Phys. Chem. C*, 2007, **111**, 3636–3641.

30 H. Liu, N. Pierre-Pierre and Q. Huo, *Gold Bull.*, 2012, **45**, 187–195.